PCCP

ROYAL SOCIETY OF CHEMISTRY

PAPER

View Article Online
View Journal | View Issue

Cite this: *Phys. Chem. Chem. Phys.*, 2024, **26**, 12379

Synergistic effect of Ag@CN with $BiVO_4$ in a unique Z-type heterojunction for enhancing photoelectrochemical water splitting performance†

Shuai Chu, Wei Zhai, Lei Ding, Lin Wang, Jie Li and Zhengbo Jiao *

Received 16th February 2024,
Accepted 8th April 2024

DOI: 10.1039/d4cp00679h

rsc.li/pccp

In the realm of photoelectrochemical technology, the enhancement of photogenerated charge carrier separation is pivotal for the advancement of energy conversion performance. Carbon nitride (CN) is established as a photocatalytic material with significant potential and exhibits unique advantages in addressing the issue of rapid recombination of photogenerated carriers. This study utilized an efficient *in situ* doping method that combined Mo,W-doped $BiVO_4$ (Mo,W:BVO) with silver-loaded CN (Ag@CN), yielding an all-solid-state Mo,W:BVO/Ag@CN heterostructure that effectively augments the separation efficiency of electron–hole pairs. Through the annealing process, Ag@CN was uniformly coated within the Mo,W:BVO thin film, significantly enlarging the interface contact area to enhance visible light absorption and photogenerated carrier movement. The results of the photoelectrochemical tests showed that the Mo,W:BVO/Ag@CN heterostructure had the highest photocurrent and charge transfer efficiency, which were 6.4 times and 3.6 times higher respectively than those of the unmodified Mo,W:BVO. Our research elucidates the interactions within all-solid-state Z-scheme heterojunctions, outlining strategic approaches for crafting innovative and superior photocatalytic systems.

Introduction

As the process of global industrialization accelerates, the consumption rate of traditional fossil fuels has risen sharply, leading to the depletion of resources and an exacerbation of environmental problems. In contrast to fossil fuels, solar energy is a clean and inexhaustible source that has always been a focal point in renewable energy research. Photoelectrochemical (PEC) technology, as an effective means of converting solar energy, is not only capable of efficiently capturing and transforming solar energy but also capable of producing chemical fuels such as hydrogen. This technology offers us a crucial avenue toward a sustainable energy future.[1–5] $BiVO_4$ (BVO) is recognized for its suitable bandgap and exceptional photoelectrocatalytic activity, making it a preferred semiconductor in hydrogen production and CO_2 reduction applications.[6–11] However, its utility has been hampered by the rapid recombination rate of photo-generated electron–hole pairs and low charge transfer rate.[12–15] To address these issues, several strategies such as surface modification, doping modification and the construction of heterostructures have been employed to optimize BVO and enhance its photocurrent density and stability.[16–23] In these strategies, the construction of heterostructures is recognized as an effective and widely implemented approach. The function of heterojunctions includes harnessing the driving force of the built-in electric field to facilitate the spatial separation of electrons and holes. This significantly prolongs the lifetime of photogenerated charge carriers, thereby providing an enhanced number of active charges for photocatalytic reactions. Within PEC processes, the strategic engineering of heterostructures is pivotal in improving the efficiency of water splitting, particularly given the oxygen evolution reaction as the rate-limiting step.[16–23]

In recent years, CN has garnered research interest due to its unique electronic structure, suitable band gap, high stability and environmental friendliness.[24,25] Despite its modest photocatalytic performance, various modification methods such as elemental doping and surface modification have been employed, significantly enhancing its photocatalytic efficiency.[26,27] For instance, J. Zou and colleagues have presented findings in which single atom Ag anchored in CN demonstrates exceptional photocatalytic activity.[28] Similarly, research conducted by Y. Cui's team has revealed that single Pt atoms anchored on g-C_3N_4 perform effectively as a co-catalyst for enhancing visible-light photocatalytic H_2 evolution and ciprofloxacin degradation.[29] Furthermore,

Institute of Materials for Energy and Environment, College of Materials Science and Engineering, Qingdao University, Qingdao, 266071, P. R. China.
E-mail: jiaozhb@163.com

† Electronic supplementary information (ESI) available: Experimental section, characterization, and other additional characterization elements. See DOI: https://doi.org/10.1039/d4cp00679h

a study led by T. Lu suggested that single Mo atom decorated polymeric CN could facilitate the efficient photocatalytic reduction of N_2.[30] These studies indicate that loading metal elements onto CN to enhance catalytic performance is a viable strategy. This composite approach can improve charge transfer and separation efficiency, changing not only the electronic state of the metal element carrier but also promoting a deeper understanding of the photocatalytic performance of the composite materials.[31]

In this study, we employed a unique synthesis method to fabricate an all-solid-state Z-scheme Mo,W:BVO/Ag@CN heterostructure aimed at enhancing the photoelectrocatalytic performance of BVO. Compared to composites with Ag, CN and Ag^+ as individual components, Mo,W:BVO with Ag@CN incorporated exhibited a higher photoelectrocatalytic performance. Under the condition of 1.23 V *vs.* RHE (AM 1.5G, 100 mW cm^{-2}), Mo,W:BVO/Ag@CN demonstrated the highest photocurrent density of 5.30 mA cm^{-2} and 84.7% charge transfer efficiency among all prepared photoanodes. We aim to provide new insights into efficient photocatalysis by conducting an in-depth study of the charge separation and transfer mechanisms within this innovative all-solid-state Z-type heterostructure.[32–37]

Results and discussion

Scheme 1 schematically illustrates the fabrication process of the Mo,W:BVO/Ag@CN heterostructure. The Ag@CN was initially synthesized using the supramolecular self-assembly method. This structure was then mixed with Mo,W:BVO precursor solution, then the mixture was drop-cast onto an FTO glass substrate. Upon drying and annealing, the photoelectrode film was successfully formed.

Fig. 1a presents the transmission electron microscope (TEM) image of Ag@CN, revealing its amorphous cluster-like structure of approximately a few hundred nanometers. Fig. 1b showcases the high-resolution TEM image of Ag@CN, displaying an absence of regularly arranged lattice stripes, implying that the CN exhibits a polycrystalline phase with defects and amorphous regions. This structure might favor the loading of Ag, facilitating the increase in the active sites for photocatalytic reactions. Furthermore, the undetected Ag nanoparticles or clusters indicated that Ag was uniformly dispersed on the CN. X-ray diffraction (XRD) analysis was utilized to elucidate the composition and crystallography of the samples. Fig. 1c pictorially represents the XRD pattern, where after discarding peaks associated with the FTO glass substrate, the identifiable peaks corresponded to monoclinic $BiVO_4$ (JCPDS 14-0688), confirming the successful synthesis of BVO. The XRD pattern of Mo,W:BVO showed no additional impurity peaks, indicating the successful substitution of vanadium ions by Mo and W ions in the BVO lattice.[38] Parallels were drawn between the XRD patterns of Ag@CN and CN, both displaying a prominent peak at a central position of 27°, corresponding to the graphite's (0 0 2) plane. This infers that Ag@CN potentially possesses an amorphous structure, capable of providing a significant abundance of active surface sites, thereby furthering Ag loading and dispersion.[39] In addition, the amorphous property of Ag@CN may constrain the lattice diffusion or agglomeration of Ag. Due to the low loading of Ag on CN, diffraction peaks associated with Ag were not observed. Upon further encapsulation of Ag@CN within Mo,W:BVO, no diffraction peaks associated with Ag@CN were detected in the XRD patterns of Mo,W:BVO/Ag@CN, likely due to the minimal addition which resulted in too weak peak intensity to be detected by the instrument.

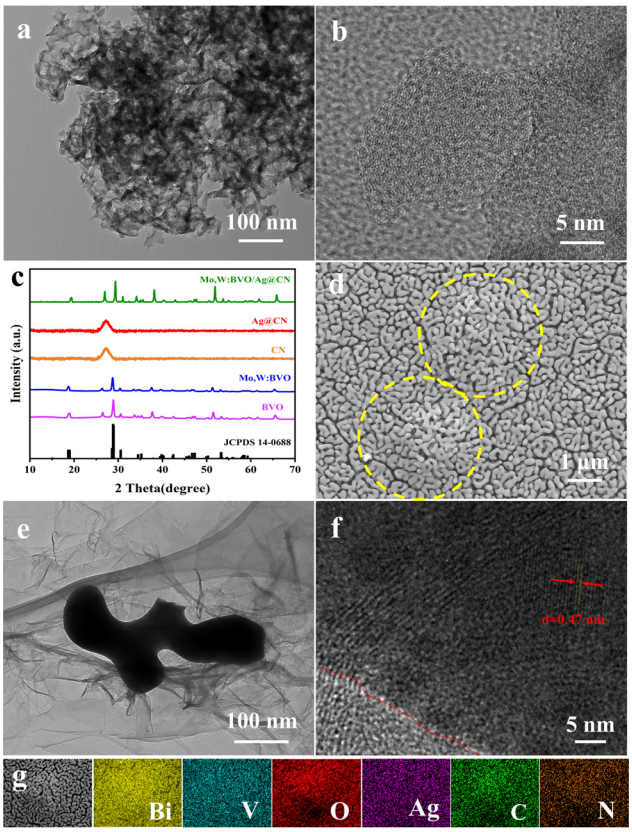

Fig. 1 Ag@CN of (a) TEM image and (b) HRTEM image; (c) XRD patterns of Mo,W:BVO/Ag@CN, BVO, Mo,W:BVO, CN and Ag@CN; Mo,W:BVO/Ag@CN of (d) SEM image, (e) TEM image, (f) HRTEM image, (g) EDS elemental mapping.

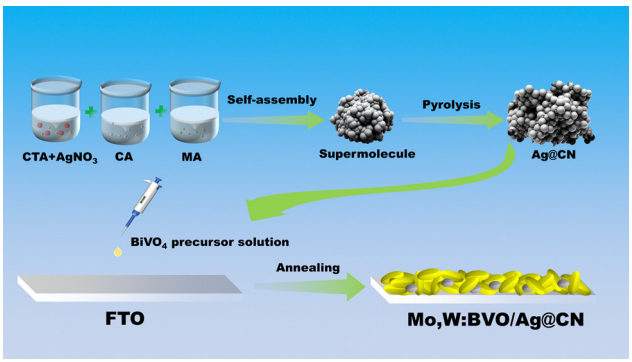

Scheme 1 Schematic illustration of the fabrication process of Mo,W:BVO/Ag@CN.

Similarly, for other BVO-based photoanodes as well, only the characteristic peaks of BVO were detected, while other related peaks went undetected (Fig. S1, ESI†). Fig. 1d displays the scanning electron microscope (SEM) images of the Mo,W:BVO/Ag@CN heterostructures. It can be observed that upon adding Ag@CN to the precursor solution of Mo,W:BVO and using the dip-coating method to apply a coating on the FTO surface, the worm-like Mo,W:BVO thin films grow flat on the FTO surface with the formation of distinct protrusions. These protrusions are outlined by yellow dashed lines. The size of the protrusions is similar to that of the Ag@CN particles, indicating that Mo,W:BVO tightly encases Ag@CN. This structure can increase the contact area between Ag@CN and Mo,W:BVO, thereby promoting the formation of the heterostructure and enhancing the efficiency of carrier transport. Further confirmation of the successful construction of the heterostructure was provided by the TEM image and high-resolution TEM image of Mo,W:BVO/Ag@CN (Fig. 1e and f), wherein the two were in close contact, underlining the stability of the formed heterostructure. Interestingly, Ag@CN exhibited a more extended flocculent shape, which was probably the result of mechanical action and ultrasonic treatment during sample preparation, increasing its contact area with Mo,W:BVO and facilitating rapid carrier transmission. Through measurement, the 0.47 nm lattice spacing corresponded to the (1 1 0) crystal face of monoclinic BVO. EDS elemental mapping spectra (Fig. 1g) further confirmed the composition of the protrusions on the BVO thin film, showing accumulation of C and N elements at the protrusion site, while Bi and V elements were primarily distributed around the periphery of the protrusion and were less present at the protrusion itself. This convincingly demonstrates that the formation of the protrusions is not due to the uneven growth of BVO but rather to the encapsulation by Ag@CN. Given the minimal content and encapsulation of Ag, its elemental distribution was not significantly detected.

A detailed exploration of the Mo,W:BVO/Ag@CN heterostructures was undertaken using X-ray Photoelectron Spectroscopy (XPS). This comprehensive analysis revealed the presence of six distinct elements, including Bi, V, O, C, N, and Ag, thereby helping to shed light on the complex interactions among these components within the heterostructures (Fig. S6, ESI†). These findings are consistent with the results obtained from EDS mapping (Fig. S4 and S5, ESI†). Further, high-resolution XPS spectra were obtained to shed light on the chemical states of these elements. The high-resolution Bi 4f spectrum (Fig. 2a) showed two distinct peaks at 159.1 eV and 164.4 eV, which correspond to Bi $4f_{7/2}$ and Bi $4f_{5/2}$ of BVO.[40] In addition, the V 2p high-resolution spectrum (Fig. 2b) revealed two characteristic peaks at 516.7 eV and 524.1 eV respectively, ascribing to V $2p_{3/2}$ and V $2p_{1/2}$, suggesting that the chemical environment of BVO remained constant even after the incorporation of Ag@CN. The O 1s spectrum (Fig. 2c) revealed that oxygen was in three distinct chemical states: 530.7 eV and 532.0 eV, which represented the surface-adsorbed hydroxyl groups and the air moisture respectively, and 529.6 eV, which associated to oxygen species within the lattice of BVO upon

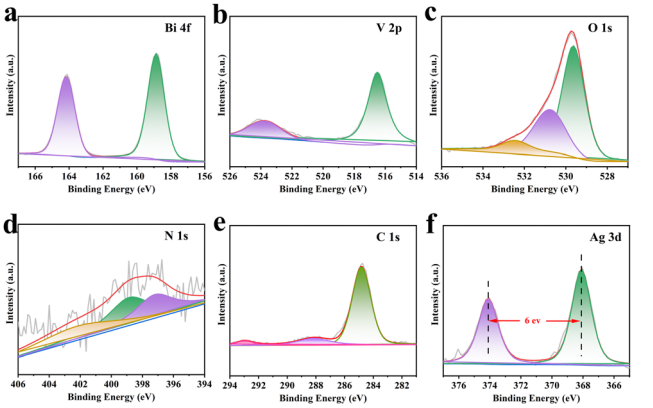

Fig. 2 XPS survey spectra of Mo,W:BVO/Ag@CN: (a) Bi 4f, (b) V 2p, (c) O 1s, (d) N 1s, (e) C 1s, (f) Ag 3d.

incorporation of Ag@CN. The characteristic peaks of N 1s were located at 397.2 eV, 398.9 eV and 402.1 eV. The N 1s peak at 397.2 eV may be attributed to –N– or –C–N–C-environments, the peak located at 398.9 eV may be ascribed to –N–O bonding, while the apex at 402.1 eV could possibly be due to highly oxidized nitrogen species originating from potential surface treatment or atmospheric exposure of the sample. Similarly, the main peaks of C 1s (Fig. 2e) showed three peaks located at 292.9 eV, 287.9 eV, and 284.9 eV, representing C–N, C–O environments, and a typical C–C or C–H environment respectively. Finally, the Ag 3d (Fig. 2f) peaks were located at 368.0 eV and 374.0 eV, corresponding to Ag $3d_{5/2}$ and Ag $3d_{3/2}$. These peaks shifted towards lower binding energy as compared to the standard Ag values (Ag $3d_{5/2}$, 368.2 eV; Ag $3d_{3/2}$, 374.2 eV), indicating prompt electron gain. Moreover, with a peak width of 6.0 eV, the presence of zero-valent Ag was suggested.[41,42]

To evaluate the PEC water splitting activity of the samples, a three-electrode system was utilized with a 0.1 M Na_2SO_4 (pH = 7) electrolyte solution. Under AM 1.5G simulated sunlight conditions, the BVO-based photoanodes were prepared and subjected to a PEC test, with the results detailed in Fig. 3. Due to the low photocurrent density of BVO, co-doping with Mo and W led to an increase in carrier density, which improved the rapid recombination bottleneck of photogenerated carriers. Consequently, the photocurrent density of Mo,W:BVO increased to 0.83 mA cm^{-2}, as illustrated in Fig. 3a. When the BVO photoanode was surface modified with Ag@CN, there was a slight enhancement in the photocurrent density. This is due to Ag's ability to capture part of the photogenerated electrons on the BVO surface under illumination, thereby minimizing the recombination rate of electron–hole pairs on the surface. Doping the system with Ag ions led to an enlargement of the photocurrent density to 3.41 mA cm^{-2}. This enhancement is likely facilitated by the introduction of impurity energy levels into the BVO band gap, which is attributed to the embedded 3d electron orbit of Ag, augmenting the system's capacity to respond to visible light.[43] Conversely, competition amongst metal ions for electrons is theorized to slow down the rate of electron–hole recombinations. After the formation of a heterojunction when Ag@CN was encapsulated

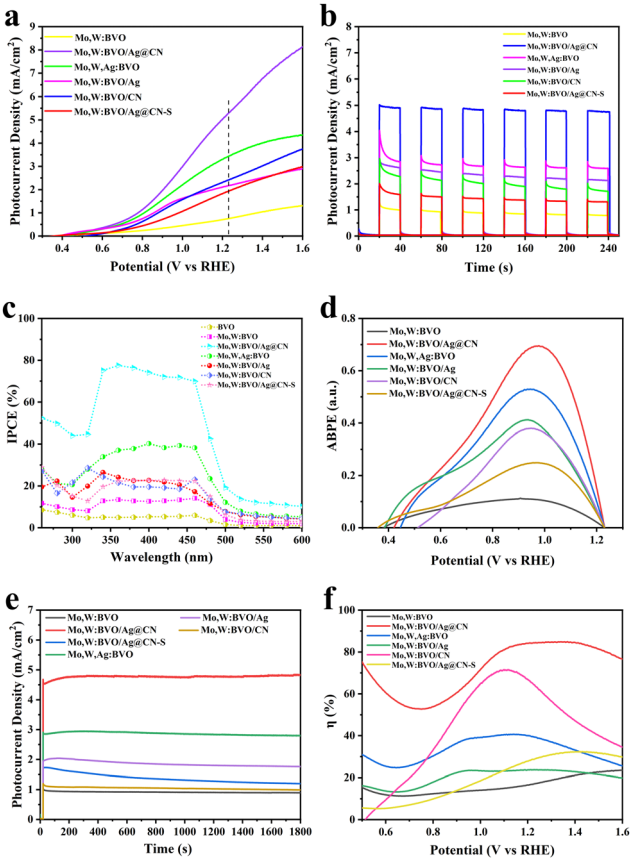

Fig. 3 (a) LSV examination, (b) *I–T* curves, (c) IPCE curves and (d) ABPE curves, (e) stability curves, (f) charge transfer efficiency of BVO-based samples.

within the BVO film, there was a dramatic surge in photocurrent density to 5.30 mA cm^{-2}. This represented a significant enhancement compared to the photocurrent densities of single-component composites Mo,W:BVO/CN and Mo,W:BVO/Ag, which were 2.20 mA cm^{-2} and 2.40 mA cm^{-2} respectively. This arguably demonstrates a synergistic interaction between CN and Ag that effectively augments photoelectric performance through the formation of a heterojunction with BVO. Based on the results of the LSV tests in the dark (Fig. S7, ESI†), we observed that the Mo,W:BVO/Ag@CN composite photoelectrode exhibited a higher current density under dark conditions. This suggests that compared to the Mo,W:BVO photoelectrode, the Mo,W:BVO/Ag@CN has a lower carrier recombination rate and better carrier separation efficiency. The *I–T* curve depicted in Fig. 3b indicates all fabricated photoanodes possessed robust transient photocurrent response capabilities, with a marginal decay in photocurrent density after six dark-light cycle exposures. The photocurrent densities of the photoanodes under different wavelengths were meticulously tested at 1.23 V *vs.* RHE, and their respective incident photon-to-current conversion efficiency (IPCE) values subsequently calculated and depicted in Fig. 3c. The IPCE value hit a peak of 77% at 360 nm when Ag@CN was encapsulated within the BVO film, far exceeding that of other photoanodes. Furthermore, the spectral absorption range of Mo,W:BVO/Ag@CN showed a clear red-shift, suggesting a considerable enhancement in incident light conversion capabilities following the encapsulation of Ag@CN, which resulted in an expanded spectral absorption range. Applied bias photon-to-electron conversion efficiency (ABPE) values were calculated based on the LSV curves obtained under simulated sunlight. As depicted in Fig. 3d, among all BVO-based photoanodes, the Mo,W:BVO/Ag@CN composite exhibited the highest ABPE of 0.7%. This value surpassesed that of other photoanodes, all of which had efficiencies under 0.6%. This indicates that the synergistic effect arising from the formation of the heterojunction between Mo,W:BVO and Ag@CN significantly enhances the photoelectric conversion capabilities of the composite structure. Fig. 3e presents the stability test curves for the prepared photoanodes. Even after 1800 s of continuous exposure to simulated sunlight, there was almost no decay in the photocurrent densities of any of the photoanodes, clearly demonstrating the exceptional light stability of these materials. This light stability is advantageous for the sustained and steady progression of photoelectrocatalytic reactions. Moreover, to further illustrate the improvement of the performance in Mo,W:BVO/Ag@CN, the charge transfer efficiency of the photoanode was calculated through the LSV curves. As depicted in Fig. 3f, the charge transfer rate of Mo,W:BVO was only 23.4%, indicating that many photogenerated electron–hole pairs did not participate in the reaction but recombined during the transmission process or on the electrode surface. In contrast, the charge transfer efficiency of Mo,W:BVO/Ag@CN reached up to 84.7%. The majority of the electron–hole pairs were able to reach the electrode surface to participate in the reaction, which suggested that the heterostructure we constructed effectively promoted charge transfer, reduced carrier recombination, and thus significantly enhanced its PEC performance.

In order to investigate the factors influencing the enhancement of photoanode photoelectric performance, and to analyze the role of Ag@CN encapsulated in BVO thin films in Mo,W:BVO/Ag@CN heterostructures, electrochemical impedance spectroscopy (EIS) tests were conducted on the prepared samples.[44] The Nyquist plot is shown in Fig. 4a, with the inset representing the equivalent circuit used during fitting. The arc shape of the Nyquist plot reflects the charge transfer dynamics, while the diameter of the semicircle represents the charge transfer resistance. From the curve, it can be seen that although the PEC performance of Mo,W:BVO significantly improved after

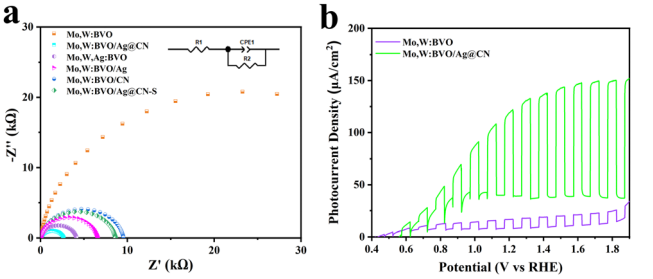

Fig. 4 (a) Nyquist plot of the EIS spectrum, (b) LSV curve under the 360 nm wavelength light of BVO-based samples.

doping with a single component, it still had a large charge transfer resistance, which hindered the reaction. However, after the modification by Ag@CN, the charge transfer resistance decreased significantly, indicating that Ag@CN on the surface could promote charge carrier transport. Among all the prepared photoanode materials, the Mo,W:BVO/Ag@CN heterostructure had the smallest charge transfer resistance, indicating the fastest rate of charge carrier migration. It is hypothesized that the encapsulated Ag@CN structure played a crucial role in enhancing the charge carrier separation and transport capabilities. Fig. 4b depicts the LSV curves tested at a wavelength of 360 nm. In comparison to Mo,W:BVO, the Mo,W:BVO/Ag@CN heterostructure showed a substantial improvement in absorbing and utilizing visible light. Additionally, the effect of Ag@CN addition on PEC performance is investigated, as shown in Fig. S8 (ESI†). Under gradient concentrations of 40, 60 and 80 μL, the LSV curves show that the PEC performance first increased and then decreased. The peak performance was reached when the addition amount was 60 μL. EDS measurements showed that the Ag content in the Mo,W:BVO/Ag@CN heterostructure was approximately 0.33% at the optimal addition amount.

The fabricated Mo,W:BVO and Mo,W:BVO/Ag@CN photoanodes underwent ultraviolet-visible diffuse reflectance testing, with results depicted in Fig. 5a. As can be seen, after encapsulation by Ag@CN, the absorption edge of Mo,W:BVO/Ag@CN photoanode was approximately at 525 nm, indicating a slight red-shift compared to the absorption edge of Mo,W:BVO at 502 nm. This expanded the range of utilizable sunlight. Due to the introduction of noble metal Ag, the overall light absorption ability was notably enhanced. The Tauc plots in Fig. 5b demonstrate that the bandgap width of Mo,W:BVO was approximately 2.41 eV, while the encapsulation of Ag@CN structure reduced the bandgap width of the composite photoanode to 2.30 eV. This allows for more thorough and efficient utilization of solar energy, which is beneficial for improving PEC performance.

To further elucidate the specific mechanisms of charge transfer within the Mo,W:BVO/Ag@CN heterostructure, free radical capture experiments were conducted on Mo,W:BVO and Mo,W:BVO/Ag@CN by degrading methylene blue (MB) under visible light. Using benzoquinone (BQ), *tert*-butanol (TBA), and ethylenediaminetetraacetic acid disodium salt (EDTA-2Na) as quenchers, which can interact with superoxide radicals ($^{\bullet}O^{2-}$), hydroxyl radicals ($^{\bullet}OH$), and holes (h^{+}) respectively, leading to the quenching of radicals and thereby identifying the predominant radical groups playing key roles in the degradation process. As shown in Fig. 5c, without the presence of a quencher, the degradation efficiency of Mo,W:BVO was 61%, which did not significantly change in the presence of BQ and EDTA-2Na. However, with TBA present, the degradation rate of MB by Mo,W:BVO was only 17%, which suggested that the primary active species in the photodegradation of Mo,W:BVO were $^{\bullet}OH$ radicals. Fig. 5d exhibits the degradation efficiency of MB by the Mo,W:BVO/Ag@CN heterostructure. In the case without a quencher, the degradation efficiency was 71%, a slight improvement compared to Mo,W:BVO. Similarly, with the addition of TBA, the degradation rate was significantly weakened. Nevertheless, in the presence of BQ, the MB degradation rate by Mo,W:BVO/Ag@CN dropped to 19%, which indicated that in the Mo,W:BVO/Ag@CN system, both $^{\bullet}OH$ and $^{\bullet}O^{2-}$ were the primary active species.

Based on the above analyses and free radical capture results, the charge transfer mechanism in the Mo,W:BVO/CN heterostructure was deduced (Scheme 2.). When BVO and CN make contact, their Fermi levels tend to equilibrate, leading to band structure changes among electron–hole pairs and thereby constructing a type II heterostructure.[45,46] However, consigning highest redox ability to the electron–hole pairs simultaneously limits the full water splitting reaction. With its superior photocatalytic properties, the Mo,W:BVO/Ag@CN heterostructure is inferred to be not a typical type II heterostructure. Following

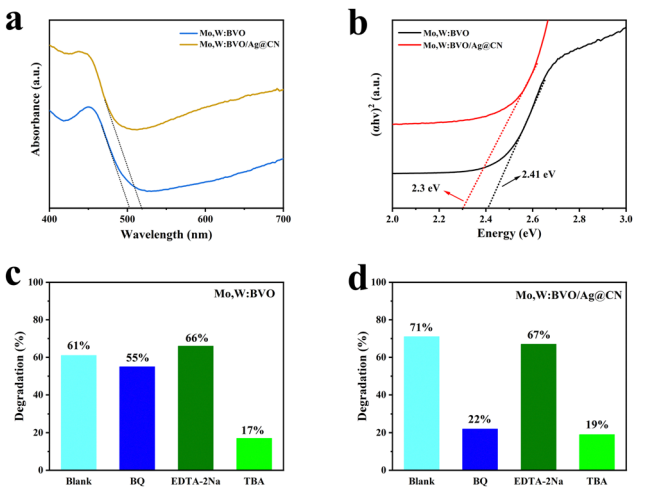

Fig. 5 UV-vis diffusive reflection spectra (a) and Tauc plot (b) of Mo,W:BVO and Mo,W:BVO/Ag@CN heterostructures. (c) Mo,W:BVO and (d) Mo,W:BVO/Ag@CN degradation MB efficiency in the presence of scavengers in visible light.

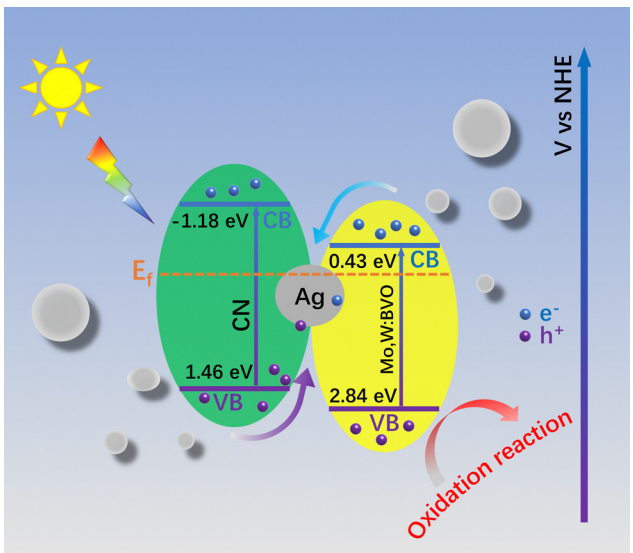

Scheme 2 Proposed mechanism for charge transferring over the Mo,W:BVO/Ag@CN heterostructure.

previous reports, the conduction band position of BVO is at 0.43 eV and the valence band position at 2.84 eV, given its bandgap of 2.41 eV. For CN, the bandgap is 2.64 eV, with the conduction band and the valence band located at −1.18 eV and 1.46 eV respectively.[28,47] Yet, the free radical capture experiments result is inconsistent with the presumed •OH generation by the hole transfer from BVO to CN as the valence band potential of CN is far more negative than the –OH/•OH redox pair. Hence, these holes are likely originating from BVO, but not CN, affirming an all-solid type Z heterostructure. After photointegration, the holes from the valence bands of CN and BVO transition to their respective conduction bands. Due to Ag's high conductivity and relatively high Fermi level, photogenerated electrons on the conduction band of BVO migrate to the grains of Ag upon reaching Fermi level balance at the BVO, Ag, and CN interface. This is consistent with the XPS test results. Moreover, the surface plasmon resonance (SPR) of Ag itself strengthens local electric fields around the interface, allowing the injected electrons to combine directly with the photo-generated holes produced on the valence band of CN.[48] In the end, the electrons on CN's conduction band transfer to the FTO substrate and then conduct to the counter electrode to generate hydrogen, while the holes on BVO's valence band transfer to the electrode surface to participate in the oxygen reduction reaction to produce oxygen. This structure not only achieves effective spatial separation of electron–hole pairs, thereby reducing carrier recombination, but also retains electron–hole pairs with a high redox potential, crucial for efficient PEC reactions. Therefore, the construction of ternary type Z structure of Mo,W:BVO/Ag@CN provides insights for the design of photoanodes with high photocatalytic activity.

Conclusions

In this study, we constructed an all-solid-state Z-type heterostructure, Mo,W:BVO/Ag@CN, by encapsulating an Ag@CN structure within a BVO film through a simple internal doping method. Compared to surface modification, the internal encapsulation of Ag@CN after structure modification ensures extensive contact with the worm-like Mo,W:BVO and facilitates a tight binding that is beneficial for the rapid transport of carriers. The presence of Ag nanoparticles as a conductive medium not only serves to eliminate non-useful photogenerated carriers, thereby reducing the rate of electron–hole recombination in the system, but also retains photogenerated carriers with strong redox potential, which is advantageous for the efficient progression of PEC water splitting reactions. PEC testing results indicate that the Z-type structure construction enhances charge transfer efficiency and effectively reduces carrier recombination, with PEC performance surpassing electrodes constructed from single components of Ag or CN combined with BVO, demonstrating a significant synergistic effect between Ag and CN. The photocurrent density of the Mo,W:BVO/Ag@CN reached 5.30 mA cm^{-2} at 1.23 V *vs*. RHE, representing a notable improvement over bare Mo,W:BVO. This research lays a foundation for the development of advanced photovoltaic heterostructures and provides a universal strategy for constructing efficient photoanode systems.

Author contributions

Wei Zhai: validation, formal analysis. Lei Ding: validation data curation. Lin Wang: validation. Jie Li: validation. Zhengbo Jiao: data curation, resources, conceptualization, writing – review & editing.

Conflicts of interest

There are no conflicts to declare.

Acknowledgements

This work was financially supported by Natural Science Foundation of Shandong Province of China (ZR2019MB006) and National Natural Science Foundation of China (21303232).

Notes and references

1 Y. Xu, Y. He, X. Cao, D. Zhong and J. Jia, *Environ. Sci. Technol.*, 2008, **42**, 2612–2617.
2 J. Wang, C. Xue, W. Yao, J. Liu, X. Gao, R. Zong, Z. Yang, W. Jin and D. Tao, *Appl. Catal., B*, 2019, **250**, 369–381.
3 S. Shyamal, A. Maity, A. K. Satpati and C. Bhattacharya, *Appl. Catal., B*, 2019, **246**, 111–119.
4 X. Fan, X. Yuan and K. Zhang, *Chin. J. Struct. Chem.*, 2024, **43**, 100207.
5 J. Miao, C. Lin, X. Yuan, Y. An, Y. Yang, Z. Li and K. Zhang, *Nat. Commun.*, 2024, **15**, 2023.
6 X. Li, T. Chen, Y. Qiu, Z. Zhu, H. Zhang and D. Yin, *Chem. Eng. J.*, 2023, **452**, 139659.
7 M. Fang, Q. Cai, Q. Qin, W. Hong and W. Liu, *Chem. Eng. J.*, 2021, **421**, 127796.
8 X. Yan, B. Wang, J. Zhao, G. Liu, M. Ji, X. Zhang, P. K. Chu, H. Li and J. Xia, *Chem. Eng. J.*, 2023, **452**, 139271.
9 C. Kim, K. M. Cho, A. Al-Saggaf, I. Gereige and H.-T. Jung, *ACS Catal.*, 2018, **8**, 4170–4177.
10 L. Zhao, J. Bian, X. Zhang, L. Bai, L. Xu, Y. Qu, Z. Li, Y. Li and L. Jing, *Adv. Mater.*, 2022, **34**, 2205303.
11 L. Sun, Z. Zhang, J. Bian, F. Bai, H. Su, Z. Li, J. Xie, R. Xu, J. Sun, L. Bai, C. Chen, Y. Han, J. Tang and L. Jing, *Adv. Mater.*, 2023, **35**, 2300064.
12 H. Irie, M. Yoda, T. Takashima and J. Osaki, *Appl. Catal., B*, 2021, **284**, 119744.
13 H. Jang, Y. Kim, H. Choi, J. Yang, Y. Jung, S. Choi, D. Lee, H. Won Jang and S. Lee, *J. Energy Chem.*, 2024, **89**, 71–78.
14 K.-A. Tsai, C.-C. Lai, Y.-H. Chen, I.-C. Leu, J.-C. Chang, C.-Y. Kuo, S.-W. Tseng, Y. Li and Y.-C. Pu, *Appl. Catal., B*, 2024, **341**, 123288.
15 C. Lin, C. Dong, S. Kim, Y. Lu, Y. Wang, Z. Yu, Y. Gu, Z. Gu, D. K. Lee, K. Zhang and J. H. Park, *Adv. Mater.*, 2023, **35**, 2209955.

16 D. H. Seo, S. Y. Hong, T. H. You, A. Sivanantham and I. S. Cho, *Chem. Eng. J.*, 2022, **450**, 137917.
17 Y. J. Jeong, S. W. Hwang, S. Chaikasetsin, H. S. Han and I. S. Cho, *Chem. Eng. J.*, 2022, **435**, 135183.
18 W. Zhang, Y. Zhang, H. Yuan, J. Li, L. Ding, S. Chu, L. Wang, W. Zhai, R. Zhu, H. Cao and Z. Jiao, *Chem. Eng. J.*, 2022, **437**, 135272.
19 Y. Xu, X. Zhang, Z. Chen, K. Kempa, X. Wang and L. Shui, *J. Mater. Sci. Technol.*, 2021, **68**, 1–7.
20 S. Jin, X. Ma, J. Pan, C. Zhu, S. E. Saji, J. Hu, X. Xu, L. Sun and Z. Yin, *Appl. Catal., B*, 2021, **281**, 119477.
21 J. Yang, Q. Shi, R. Zhang, M. Xie, X. Jiang, F. Wang, X. Cheng and W. Han, *Carbon*, 2018, **138**, 118–124.
22 H. S. Han, S. Shin, D. H. Kim, I. J. Park, J. S. Kim, P.-S. Huang, J.-K. Lee, I. S. Cho and X. Zheng, *Energy Environ. Sci.*, 2018, **11**, 1299–1306.
23 H. Zhang, H. Li, Z. Wang, Z. Zheng, P. Wang, Y. Liu, X. Zhang, X. Qin, Y. Dai and B. Huang, *Appl. Catal., B*, 2018, **238**, 586–591.
24 H. Yang, D. He, T. Zhang, C. Liu, F. Cheng, Y. Zhou, Y.-N. Zhang and J. Qu, *Chem. Eng. J.*, 2023, **466**, 143309.
25 J. Lin, W. Tian, H. Zhang, X. Duan, H. Sun, H. Wang, Y. Fang, Y. Huang and S. Wang, *J. Hazard. Mater.*, 2022, **434**, 128866.
26 K. Chen, X. Wang, Q. Li, Y.-N. Feng, F.-F. Chen and Y. Yu, *Chem. Eng. J.*, 2021, **418**, 129476.
27 X. Miao, B. Wang, H. Fan, P. Zhang, S. Bai and W. Liu, *Chem. Eng. J.*, 2023, **465**, 142775.
28 X. H. Jiang, L. S. Zhang, H. Y. Liu, D. S. Wu, F. Y. Wu, L. Tian, L. L. Liu, J. P. Zou, S. L. Luo and B. B. Chen, *Angew. Chem., Int. Ed.*, 2020, **59**, 23112–23116.
29 J. Wu, Y. Cui, X. Li, I. Khan, X. Liu, Y. Xu, Y. Song and H. Xie, *Int. J. Hydrogen Energy*, 2024, **51**, 1138–1150.
30 X.-W. Guo, S.-M. Chen, H.-J. Wang, Z.-M. Zhang, H. Lin, L. Song and T.-B. Lu, *J. Mater. Chem. A*, 2019, **7**, 19831–19837.
31 H. Starukh, M. Koštejn, V. Matějka and P. Praus, *Nanoscale Res. Lett.*, 2021, **16**, 166.
32 H. Park, N. Son, B. H. Park, C. Liu, S. W. Joo and M. Kang, *Chem. Eng. J.*, 2022, **430**, 133104.
33 N. Li, J. Wang, G. Zhao, J. Du, Y. Li, Y. Bai, Z. Li and Y. Xiong, *ACS Mater. Lett.*, 2024, **6**, 999–1006.
34 D. Pan, Y. Lu, A. M. Idris, Z. Chen, L. Xu, J. Wang, G. Jiang, Z. Chen and Z. Li, *J. Mater. Chem. A*, 2024, DOI: **10.1039/D3TA07842F**.
35 F. Wang, S. Zhang, W. Jing, H. Qiu, Y. Liu and L. Guo, *J. Mater. Sci. Technol.*, 2024, **189**, 146–154.
36 Z. Jin, X. Zheng, Z. Zhu, C. Jiang, S. Wu, C. Hu, L. Liu, L. Fang and Z. Cheng, *Nano Energy*, 2024, **122**, 109284.
37 J. Lauwaert and N. T. Jacob, *Small*, 2024, 2307712.
38 J. Li, J. Li, H. Yuan, W. Zhang, Z. Jiao and X. Song Zhao, *Chem. Eng. J.*, 2020, **398**, 125662.
39 F. Raziq, Y. Qu, M. Humayun, A. Zada, H. Yu and L. Jing, *Appl. Catal., B*, 2017, **201**, 486–494.
40 D.-K. Ma, M.-L. Guan, S.-S. Liu, Y.-Q. Zhang, C.-W. Zhang, Y.-X. He and S.-M. Huang, *Dalton Trans.*, 2012, **41**, 5581–5586.
41 D. Lin, H. Wu, R. Zhang and W. Pan, *Chem. Mater.*, 2009, **21**, 3479–3484.
42 D. Cheng, Y. Zhang, C. Yan, Z. Deng, X. Tang, G. Cai and X. Wang, *J. Mol. Liq.*, 2021, **338**, 116639.
43 B. Zhang, H. Zhang, Z. Wang, X. Zhang, X. Qin, Y. Dai, Y. Liu, P. Wang, Y. Li and B. Huang, *Appl. Catal., B*, 2017, **211**, 258–265.
44 J. Zheng, S. Xu, J. Sun, J. Zhang, L. Sun, X. Pan, L. Li and G. Zhao, *Appl. Catal., B*, 2023, **338**, 123056.
45 A. S. Kshirsagar and P. K. Khanna, *Mater. Chem. Front.*, 2019, **3**, 437–449.
46 H. Cai, B. Wang, L. Xiong, J. Bi, L. Yuan, G. Yang and S. Yang, *Appl. Catal., B*, 2019, **256**, 117853.
47 M. Song, Y. Wu, C. Du and Y. Su, *J. Colloid Interface Sci.*, 2021, **588**, 357–368.
48 Z. Li, Z. Wang, J. Li, Q. Zhu, Z. Wang and Z. Dai, *J. Am. Chem. Soc.*, 2021, **143**, 13478–13482.